UNIVERSITY *of York*

This is a repository copy of *Characterization of two photon excited fragment spectroscopy (TPEFS) for HNO3 detection in gas-phase kinetic experiments*.

White Rose Research Online URL for this paper:
https://eprints.whiterose.ac.uk/177038/

Version: Published Version

Article:

White Rose
university consortium
Universities of Leeds, Sheffield & York

eprints@whiterose.ac.uk
https://eprints.whiterose.ac.uk/

Characterization of two photon excited fragment spectroscopy (TPEFS) for HNO₃ detection in gas-phase kinetic experiments†

Damien Amedro, Arne J. C. Bunkan, Terry J. Dillon and John N. Crowley ⬥ *

We have developed and tested two-photon excited fragment spectroscopy (TPEFS) for detecting HNO₃ in pulsed laser photolysis kinetic experiments. Dispersed (220–330 nm) and time-dependent emission at (310 ± 5) nm following the 193 nm excitation of HNO₃ in N₂, air and He was recorded and analysed to characterise the OH(A²Σ) and NO(A²Σ⁺) electronic excited states involved. The limit of detection for HNO₃ using TPEFS was ∼5 × 10⁹ molecule cm⁻³ (at 60 torr N₂ and 180 µs integration time). Detection of HNO₃ using the emission at (310 ± 5 nm) was orders of magnitude more sensitive than detection of NO and NO₂, especially in the presence of O₂ which quenches NO(A²Σ⁺) more efficiently than OH(A²Σ). While H₂O₂ (and possibly HO₂) could also be detected by 193 nm TPEFS, the relative sensitivity (compared to HNO₃) was very low. The viability of real-time TPEFS detection of HNO₃ using emission at (310 ± 5) nm was demonstrated by monitoring HNO₃ formation in the reaction of OH + NO₂ and deriving the rate coefficient, k_2. The value of k_2 obtained at 293 K and pressures of 50–200 torr is entirely consistent with that obtained by simultaneously measuring the OH decay and is in very good agreement with the most recent literature values.
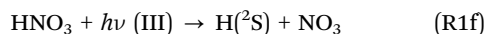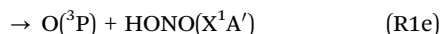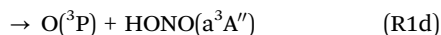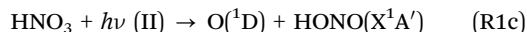
1. Introduction

HNO₃ is an important atmospheric trace gas and its ultra-violet photo-dissociation has been the subject of numerous studies.[1] The photo-dissociation of HNO₃ can be divided into three channels, leading to formation of OH, O-atoms or H-atoms, the relative importance of which depends on the wavelength.

$$HNO_3 + h\nu \text{ (I)} \rightarrow OH(X) + NO_2(X^2A_1) \quad \text{(R1a)}$$

$$\rightarrow OH(X) + NO_2(1^2B_2) \quad \text{(R1b)}$$

$$HNO_3 + h\nu \text{ (II)} \rightarrow O(^1D) + HONO(X^1A') \quad \text{(R1c)}$$

$$\rightarrow O(^3P) + HONO(a^3A'') \quad \text{(R1d)}$$

$$\rightarrow O(^3P) + HONO(X^1A') \quad \text{(R1e)}$$

$$HNO_3 + h\nu \text{ (III)} \rightarrow H(^2S) + NO_3 \quad \text{(R1f)}$$
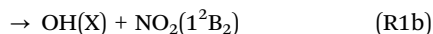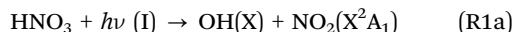
At wavelengths (λ) greater than 250 nm, the n–π* transition (to the 1 ¹A″ electronic excited state) in HNO₃ leads to photo-dissociation into predominantly OH + NO₂ ($\Phi^I_{250nm} > 0.97$) with a weak contribution from O-atom formation ($\Phi^{II}_{250nm} = 0.03$). The formation of NO₃ and H photo-fragments (Channel III)

Division of Atmospheric Chemistry, Max Planck-Institut für Chemie, 55128, Mainz, Germany. E-mail: john.crowley@mpic.de

† Electronic supplementary information (ESI) available. See DOI: 10.1039/d1cp00297j

at these wavelengths has been assigned an upper limit of $\Phi^{III}_{250nm} < 0.012$.[2]

At $\lambda < 250$ nm, HNO₃ is excited to the 2¹A′ electronic excited through an π–π* transition. At 193 nm, channel II becomes the main photo-dissociation channel with quantum yields of $\Phi^{II}_{193nm} = 0.67$ and $\Phi^I_{193nm} = 0.33$.[2–5] OH fragments formed in channel I are produced in their vibrational ground state with little rotational excitation,[6–9] whereas the NO₂ co-fragment is formed either in its ground state, or in its 1²B₂ electronically excited state (yield < 1.0%). The ground state NO₂ thus formed is sufficiently energy rich to decompose to NO and O(³P). Experimental determinations of the yield of O(¹D) in channel II vary between 0.54 and 0.28.[2,5] At shorter wavelengths, $\lambda < 155$ nm, OH can be formed in an electronically excited state[10,11] in a single photon process.

In a series of papers by Stuhl and co-workers studying the excitation of HNO₃ at 193 nm,[12–14] it was shown that electronically excited OH, OH(A), was produced in a sequential, two-photon process. From experimental observations, spin conservation and energy considerations the authors were able to demonstrate that OH(A) was not formed directly but *via* the photolysis of electronically excited HONO, probably in its metastable lower triplet state (a³A″). They used these findings to develop a new method (laser-photolysis fragment-fluorescence, LPFF) for the measurement of HNO₃ in the atmosphere.[15,16] Recently, Winiberg *et al.*[17] reported results

from the multi-photon photolysis of HNO₃ at 193 and 248 nm and reported dispersed OH and NO fluorescence spectra. They demonstrated that OH emission from a 2-photon excitation of HNO₃ was not only observed upon excitation at 193 nm but also at 248 nm. In a previous study[18] from our group (on the reaction between OH and HNO₃), the TPEFS method was used to check for HNO₃ concentration gradients across the reactor at low temperature (220 K < T < 250 K).

In this paper, we investigate the two-photon photodissociation of HNO₃ at 193 nm and demonstrate the application of two-photon excited fragment spectroscopy (TPEFS) detection of HNO₃ in real-time (flash photolysis) kinetic studies. For the latter we re-measured the well-known rate coefficient[19,20] of the reaction between OH and NO₂ (R2) by monitoring the HNO₃ product by TPEFS and also by near-simultaneous detection of OH *via* Laser Induced Fluorescence (LIF):

$$OH + NO_2 + M \rightarrow HNO_3 + M \qquad (R2a)$$

$$\rightarrow HOONO + M \qquad (R2b)$$

The three-body association reaction of OH with NO₂ is known to proceed *via* two product channels ((R2a) and (R2b)) forming mainly nitric acid (HNO₃) but with a contribution from peroxynitrous-acid (HOONO).[21,22] At room temperature and a pressure of 100 mbar the rate coefficients of the two reactions have been evaluated as: $k_{2a} = 3.0 \times 10^{-12}$ cm³ molecule⁻¹ s⁻¹ and $k_{2b} = 2.0 \times 10^{-13}$ cm³ molecule⁻¹ s⁻¹. [23] HOONO is thermally unstable with a room-temperature lifetime w.r.t. decomposition to OH + NO₂ of ≈10 s. However, on the milli-second timescale of our experiments it can be considered a stable product. As the application of TPEFS in kinetic studies of HNO₃ will depend on its selectivity, we characterisd the sensitivity of TPEFS at 193 nm for detection of several other trace gases, including NO and NO₂ which are often present (as impurities or products) in reaction systems involving HNO₃.

2. Experimental

All measurements were performed at 293 K on the PLP-LIF apparatus shown in Fig. 1. Several features of the setup have been described in detail elsewhere.[24] The main modifications to the present set-up are (1) the incorporation of a gated CCD camera for dispersed fluorescence measurement and (2) an additional (193 nm) excimer laser.

2.1 Radical generation, fluorescence excitation and detection

Laser-light is coupled in/out of the thermostatted, multi-axis reaction cell (volume ∼500 cm³) *via* Brewster-angle quartz windows. Pulsed (∼20 ns) 248 nm light from a KrF-excimer laser (Coherent COMPex 205F) provided a source of OH radicals (*e.g. via* H₂O₂ photolysis, see later).

HNO₃ was detected following excitation/dissociation at 193 nm using an ArF excimer laser (Coherent COMPex Pro 201F). A focal lens (f = 50 cm) was used to mildly focus the laser in the middle of the reactor to enhance the HNO₃ detection sensitivity. Typical photon fluxes at 193 nm varied from
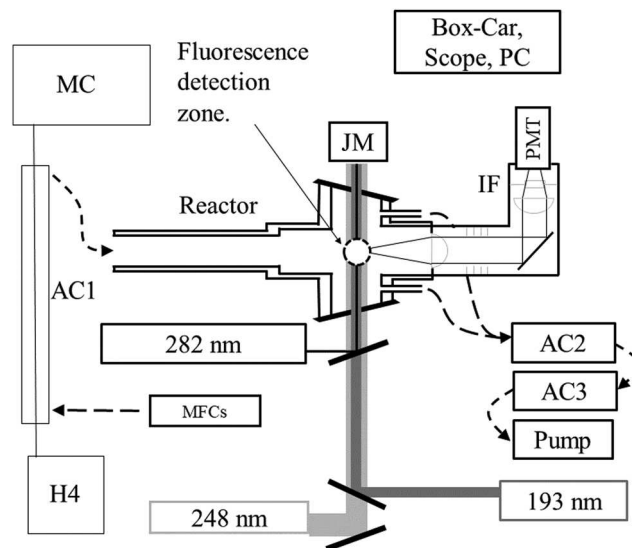

Fig. 1 Schematic of the combined PLP-LIF and PLP-TPEFS set-up. PMT: photomultiplier, IF: interference filter, AC1: absorption cell with l = 110 cm (240–400 nm), AC2: absorption cell with l = 34.8 cm (213.86 nm): AC2: absorption cell with l = 43.8 cm (184.95 nm). MC: monochromator with diode-array detector. H4: Halogen lamp. 193, 248 and 282 nm pulses were provided by excimer lasers and a YAG-pumped dye-laser, respectively. Dispersed fluorescence was collected on an axis orthogonal to the page using a lens/optical-fibre set-up. Dashed lines indicate direction of gas-flow.

30 to 50 mJ cm⁻² (measured at the exit of the photolysis cell). OH was excited at 282 nm using a YAG-pumped Dye-Laser (Quantel Brilliant B/Lambda-Physik ScanMate II). All three lasers operated at 10 Hz. The PMT signal was accumulated using either a box-car integrator (Stanford Research Systems, SR 250) for kinetic measurements or a digital oscilloscope (Tektronix TDS 3014C, 100 MHz) for recording time-resolved fluorescence signals.

The fluorescing volume at the reactor centre was imaged *via* a 5 cm diameter quartz lens on the major axis of the cell onto a photomultiplier tube screened with a 280 nm long-pass filter (BG26) and a (310 ± 5) nm interference filter. A lens/optical fibre set up on an orthogonal axis transmitted fluorescence from the same volume to the entrance slit of a 0.5 m mono-chromator (Acton Research 500) equipped with a gated, intensified CCD camera (Roper Scientific, PMax) for measurement of dispersed fluorescence. Spectra were recorded using gratings with either 300 or 1200 lines mm⁻¹ resulting in spectral ranges of ∼80 nm (at ∼1.2 nm resolution) or ∼20 nm (at ∼0.4 nm resolution), respectively. Spectral resolution determination and wavelength calibration was carried out using a low pressure Hg-lamp.

2.2 Reagent gas concentrations

The concentrations of reagent gases were monitored using three different, on-line optical absorption set-ups. Absorption by NO₂ (400–450 nm) was measured in an absorption cell (l = 110 cm) using a halogen lamp as light source and a 0.5 m monochromator/diode array camera as detector. NO₂ concentrations

6398 | *Phys. Chem. Chem. Phys.*, 2021, **23**, 6397–6407

This journal is © the Owner Societies 2021

were derived by least-squares fitting to a literature reference spectrum degraded to the same resolution.[25] The concentration of H_2O_2 was determined from its optical absorption at 213.86 nm (low pressure Zn-lamp, l = 34.8 cm) using an absorption cross-section of $\sigma_{213.9}(H_2O_2) = 3.3 \times 10^{-19}$ cm^2 molecule^{-1}.[26] The concentrations of HNO_3 and H_2O were determined from their optical absorption at 184.95 nm (low pressure Hg-lamp, l = 43.8 cm) using $\sigma_{184.95}(HNO_3) = 1.63 \times 10^{-17}$ cm^2 molecule^{-1}[18,27,28] and $\sigma_{184.95}(H_2O) = 7.14 \times 10^{-20}$ cm^2 molecule^{-1}.[29] In the same set-up, the ozone concentration was measured at 253.65 nm using a cross-section of 1.1×10^{-17} cm^2 molecule^{-1}.[23]

2.3 Chemicals

Bottled N_2 (Westfalen, 5.0) was used without further purification. H_2O_2 (AppliChem, 50 wt%) was concentrated by vacuum distillation. NO_2 was prepared by reacting ∼50 torr of NO with a large excess of O_2 in a dried glass bulb. The NO_2 was then condensed at liquid N_2 temperature and excess O_2 and NO were removed by pumping. The resulting NO_2 was stored as a mixture of 5% NO_2, 10% O_2 and 85% N_2. Anhydrous nitric acid was prepared by mixing KNO_3 (Sigma Aldrich, 99%) and H_2SO_4 (Roth, 98%), and condensing the HNO_3 vapour into a liquid nitrogen trap. Anhydrous nitric acid was kept at 252 K between experiments.

3. Results and discussion

3.1 Fluorescence from HNO_3 at (310 ± 5) nm in N_2

Our TPEFS measurement of HNO_3 monitors a fluorescence signal that is transmitted through an interference filter (310 ± 5 nm) that biases detection to the strong OH (0,0) emission lines. Fig. 2 (upper panel) displays the averaged (500 laser pulses), time-resolved signal due to three different concentrations of HNO_3 (in a flow of N_2 at a total pressure of 100 torr) which were quantified by absorption at 184.95 nm. The integrated fluorescence signals are plotted against HNO_3 concentration in the lower panel of Fig. 2 which indicates that, for $[HNO_3]$ up to 2×10^{14} molecule cm^{-3} and under these experimental settings (PMT voltage, focused 193 nm laser light), the fluorescence signal is proportional to $[HNO_3]$. At 60 torr N_2, we achieved a limit of detection for HNO_3 of 5×10^9 molecule cm^{-3} at 1σ for 2 min of signal accumulation, which results (at 10 Hz) in a total signal integration time of 180 μs.

The dependence of the TPEFS signal on the 193 nm laser energy (E_{193nm}, varied by changing the high-voltage of the excimer laser or placing fine metal mesh in the beam at the exit of the laser) is displayed in Fig. 3. The relative change in energy was measured by splitting part of the laser-beam to a photo-diode with a linear response in the range measured.

The signal does not follow the expected quadratic dependence on laser energy for a two-photon process, but varies linearly, with a negative offset. This is a result of saturation of the first electronic transition due to the focused 193 nm radiation and the large absorption cross-section of HNO_3. The apparent, negative offset is
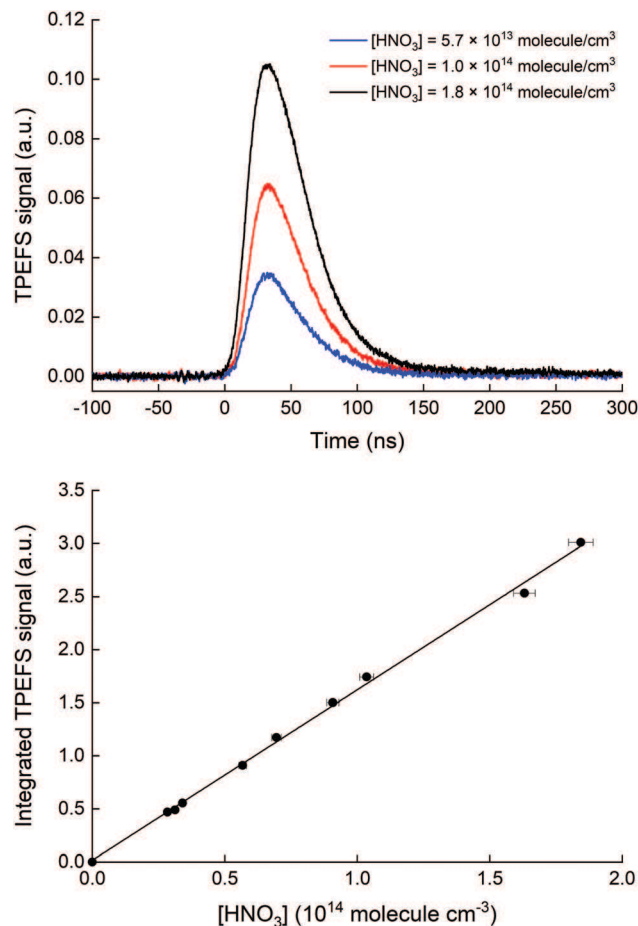
Fig. 2 Upper panel: Time resolved fluorescence signal detected by the PMT and (310 ± 5) nm interference filter at 100 torr N_2 and room temperature (298 ± 2 K). Lower panel: TPEFS signal (0–150 ns) versus HNO_3 concentration. The straight line is a linear regression to the data.

Fig. 3 TPEFS signal as a function of 193 nm laser energy. The solid line is a linear regression. The experimental conditions were: 100 torr $[N_2]$ and $[HNO_3]$ = 1.1×10^{13} molecule cm^{-3}.
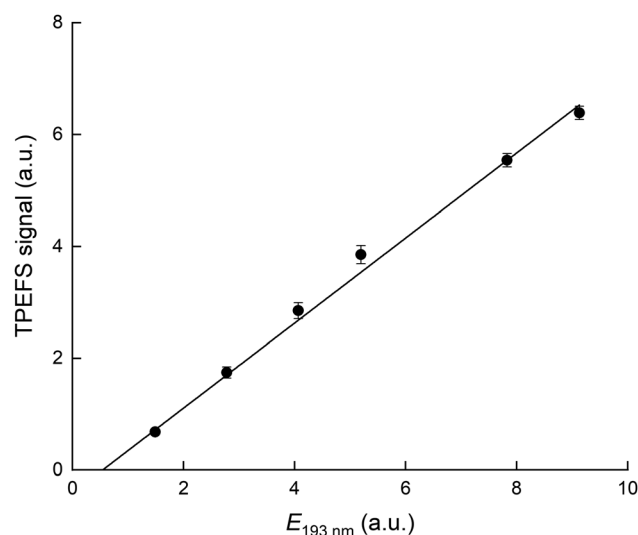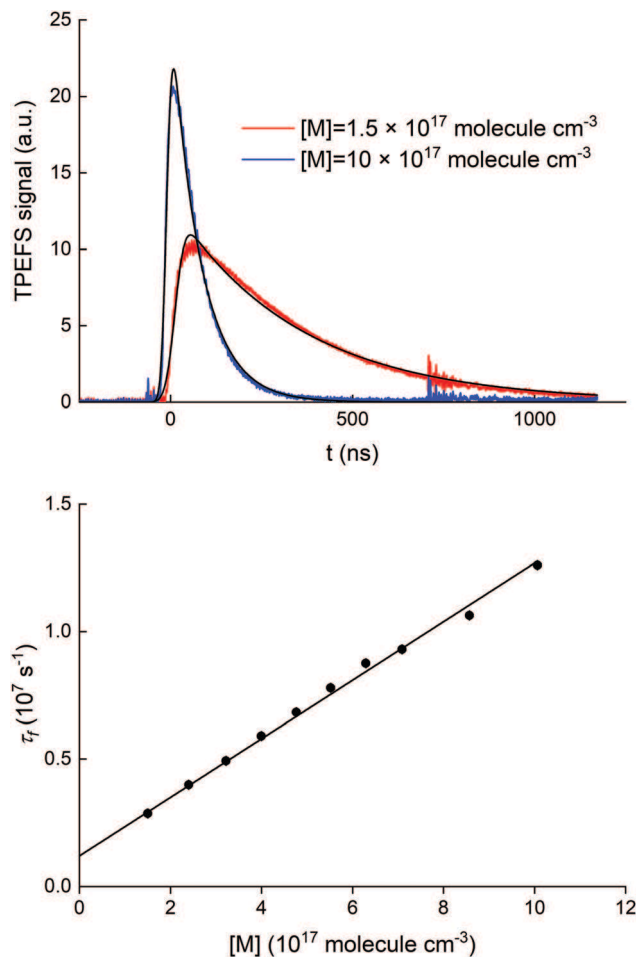
Fig. 4 Upper panel: Time resolved fluorescence signal detected by the PMT through the (310 ± 5) nm interference filter following the 193 nm excitation of HNO_3. The black, solid lines correspond to fits using (E2). Lower panel: Fluorescence decay constant (τ_f) versus bath gas (N_2) concentration. The black solid line corresponds to a linear regression used for fitting τ_f. Error bars are 2σ statistical only.

a manifestation of non-linearity at low laser energy where the first transition is not yet saturated. Our energy dependence contrasts that reported by Winiberg et al.[17] who observed a quadratic dependence on laser fluence. This difference is likely related to their use of much lower laser fluences (factor ~ 15) and (potentially) a less focused laser beam.

A series of auxiliary experiments was conducted to examine the quenching of the fluorescence by N_2. The fluorescence signals, recorded for $[HNO_3] = 5.0 \times 10^{12}$ molecule cm^{-3}, at N_2 densities between 1.5 and 10×10^{17} molecule cm^{-3} (~ 4 and ~ 30 torr at 293 K), are displayed in the upper panel of Fig. 4.

Assuming that the fluorescence corresponds to the (0,0) transition from the OH(A) state we can write:

$$d[OH(A)]/dt = k_f + k_q(N_2)[N_2] + k_q(HNO_3)[HNO_3] \quad (1)$$

where k_f is the fluorescence decay rate constant (s^{-1}) and is the inverse of the radiative lifetime, τ_f. $k_q(N_2)$ is the quenching rate constant for N_2 bath gas, $k_q(HNO_3)$ is the quenching rate constant for HNO_3 (k_q in units of cm^3 molecule^{-1} s^{-1}),

$[HNO_3]$ and $[N_2]$ are the concentrations of HNO_3 and N_2 (both in molecule cm^{-3}). The fluorescence profiles in Fig. 4 were fitted to eqn (E2), which is a convolution of a Gaussian function and a simple exponential decay:

$$S = S_0 \exp\left(\left(\frac{\alpha^2}{\beta^2}\right) - \frac{(t - t_0)}{\beta}\right) \times \left(1 - \mathrm{erf}\left(\alpha^2 - \frac{\beta \times (t - t_0)}{\sqrt{2} \times \alpha \times t}\right)\right)$$
$$(2)$$

where S_0 is the signal intensity, α (s) is the width of the Gaussian function, β is the fluorescence decay lifetime in s and thus the reciprocal of the decay constant (τ_f), t_0 is the time (s) at the onset of the signal rise and erf is the error function. This equation allows us to account for the finite pulse width of the 193 nm excimer laser (~ 20 ns), the response time for the PMT (~ 20 ns) and the oscilloscope bandwidth (100 MHz) which result in non-instantaneous build-up of signal. The slope of the plot of τ_f versus $[N_2]$ (lower panel of Fig. 4), is the quenching rate constant, here determined as $k_q(N_2) = (1.1 \pm 0.1) \times 10^{-11}$ cm^3 molecule^{-1} s^{-1}. This is in good agreement with the value of $(1.3 \pm 0.4) \times 10^{-11}$ cm^3 molecule^{-1} s^{-1} reported by Kenner et al.[14] for collisional deactivation of rotational levels $N' = 1$–16 of the $v' = 0$ state of OH(A) generated by the 193 nm excitation of HNO_3. It is approximately 3 times smaller than those derived from experiments in which OH(A, $v' = 0$) was formed rotationally cold ($N' < 4$)[30,31] and thus in qualitative agreement with previous observations that the electronic quenching rate coefficient decreases as the rotational level increases.[32,33]

At an HNO_3 concentration of 5×10^{12} molecule cm^{-3} and using the quenching rate constant reported by Kenner et al.[14] of $k_q(HNO_3) = 5.9 \times 10^{-10}$ cm^3 molecule^{-1} s^{-1}, we calculate $k_q(HNO_3)[HNO_3] \approx 3000$ s^{-1} which thus represents a negligible contribution ($<1\%$) to the intercept of $(1.2 \pm 0.1) \times 10^6$ s^{-1}. The inercept can thus be equated to k_f and results in a radiative lifetime of about (840 ± 90) ns (errors are 2σ statistical). This value is somewhat larger than the natural fluorescence lifetime of (688 ± 21) ns[34] for the $A^2\Sigma(v' = 0) \rightarrow X^2\Pi(v'' = 0)$ transition, indicating that the nascent OH($A^2\Sigma(v' = 1,2)$) formed from 193 nm, two-photo excitation of HNO_3 undergoes vibrational energy transfer down to $A^2\Sigma(v' = 0)$ on the same timescale as the fluorescence emission and the electronic quenching. This was confirmed by the observation of an increase in the signal intensity as the pressure was increased although $[HNO_3]$ was kept constant.

3.2 Dispersed fluorescence spectrum of HNO_3

In Fig. 5 we display the emission spectrum (220 to 330 nm) obtained in the excitation of HNO_3 at 193 nm in He bath gas at 90 torr. The individual spectra for each ~ 20 nm wide spectral region are the average of 2000 single spectra (obtained at 10 Hz) with a gate width (i.e. CCD exposure time) of 1 μs and were recorded 45 ns after the 193 nm laser pulse. The features are assigned to emission from excited OH and NO. Note that the final spectrum is not corrected for the wavelength dependent sensitivity of the detector or wavelength dependent transmission
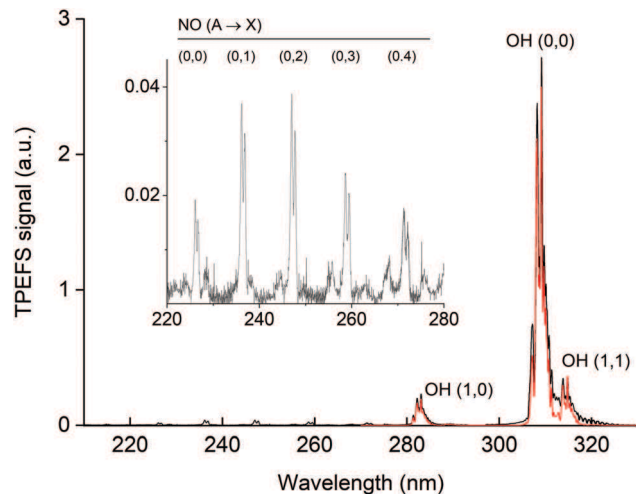
Fig. 5 Fluorescence emission spectrum (black line) following excitation of 7×10^{13} molecule cm^{-3} HNO$_3$ in 90 torr He at 193 nm. The inset has an expanded y-scale showing NO fluorescence emission lines from 220 to 280 nm. The red line is a simulation (LIFBASE[35]) of the relative line intensities for the OH A$^2\Sigma$(v' = 0,1,2) → X$^2\Pi$(v''= 0,1,2) transition using T_{vib} = 3200 K and T_{rot} = 700 K.

of either the monochromator or the optical fibre used. This will result in a positive bias to longer wavelength fluorescence and thus features such as the NO emission lines between 225 and 280 nm are stronger (relative to the OH(A) lines) than depicted in this figure. Under these experimental conditions, we were able to observe the OH(0,0) emission centred at 310 nm and emissions of vibrationally excited OH at ~282 nm OH(1,0), ~287 nm OH(2,1) and ~315 nm OH(1,1).

Using LIFBASE[35] we could approximately reproduce the measured OH fluorescence spectra with a vibrational temperature (T_{vib}) of ~3200 K and a rotational temperature (T_{rot}) of ~700 K. The former value is in qualitative agreement with Kenner et al.[14] who also observed a high degree of vibrational excitation in OH and reported a vibrational temperature of 375 K.

The NO emission lines have been observed previously in the 193 nm excitation of HNO$_3$ and were thought to be the result of the excitation of NO$_2$, which was present as an impurity in the experiments of Papenbrock et al.[12] However, our measurement of the NO* fluorescence emission resulting from the excitation of NO$_2$ at 193 nm (see Fig. 6) showed that the intensities of the NO emission lines are much smaller than those observed in the excitation of similar amounts of HNO$_3$, which leads us to conclude that NO* is formed via 193 nm excitation of HNO$_3$ and not from NO$_2$ impurity.

Indeed, this additional channel, in which the co-product would be OH in its electronic ground state, is energetically feasible and has been proposed previously.[36] Recent work by Winiberg et al.[17] also showed that NO(A) was observed from the two photon photolysis of HNO$_3$ at 248 nm.

3.3 TPEFS detection of selected NO$_X$ and HO$_X$ trace gases

In this section we discuss the relative detection sensitivity of TPEFS to HNO$_3$, NO and NO$_2$. The results are summarised in
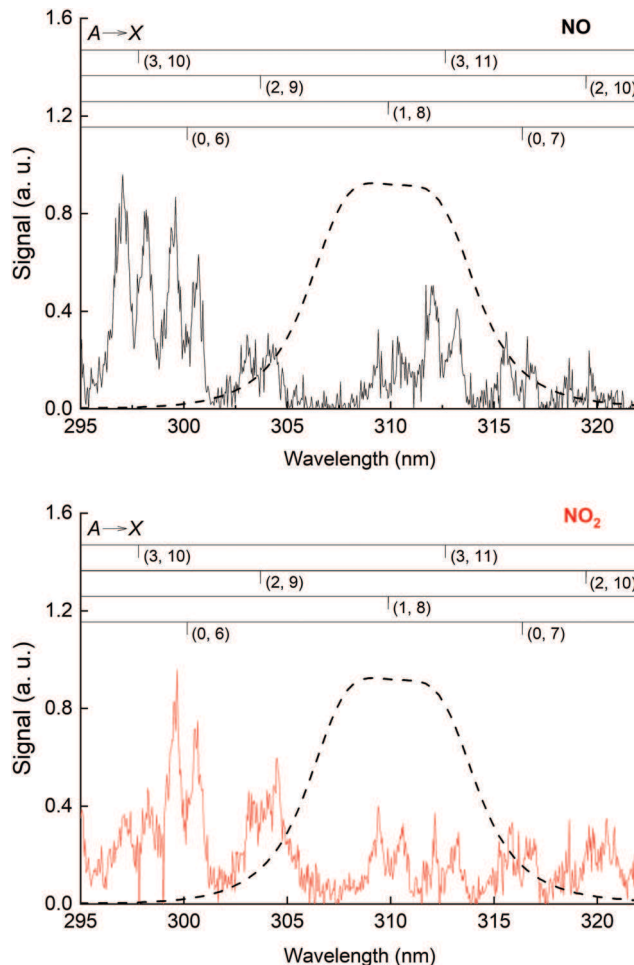

Fig. 6 Upper panel: NO fluorescence emission spectrum following 193 nm excitation of NO with assignment to vibrational transitions from the A to X electronic states. Lower panel: As upper panel but following 193 nm NO$_2$ excitation. Experiments were carried out at ~298 K and a bath gas-pressure of 60 torr (N$_2$) with [NO] = 3.0×10^{15} molecule cm^{-3} or [NO$_2$] = 2.4×10^{15} molecule cm^{-3}. The 310 nm interference filter transmission curve (used for selective detection of emission from OH(A)) is represented by the dashed line.

Table 1. As described above, the NO(A) emission lines seen when exciting HNO$_3$ samples at 193 nm may arise from the presence of impurities such as NO or NO$_2$. Here, we examine the relative detection sensitivity for NO and NO$_2$, identify the origin of these lines and assess the potential interference of NO and NO$_2$ whilst monitoring HNO$_3$ as OH(A).

Table 1 TPEFS sensitivity (S) to NO, NO$_2$, HO$_2$ and H$_2$O$_2$

	HNO$_3$	NO	NO$_2$	H$_2$O$_2$	HO$_2$
σ^a	1100[23]	<0.001	29[37]	61[23]	390[38]
S (N$_2$)	10 000	(30 ± 10)	(50 ± 20)	—	<(3 ± 1)
S (air)	10 000	(5 ± 1)	—	(0.6 ± 0.2)	
S (He)	10 000	<1	—	—	

^{a} σ is the single-photon absorption cross-section at 193 nm (units of 10^{-20} cm^2 molecule^{-1}). Detection sensitivity is relative to HNO$_3$. Uncertainties are 2σ statistical only.

For both NO and NO_2, we performed a series of experiments in different bath gases (N_2 and He) and with and without O_2 in order to assess the excitation mechanism at the origin of emission around 310 nm. To minimize HNO_3 interference from NO and NO_2 excitation spectra, we coated the gas line leading to the reactor with $NaHCO_3$. The removal of HNO_3 was confirmed by the non-observation of OH emission lines.

In experiments designed to investigate the kinetics of HNO_3 formation *via* the reaction between OH and NO_2 (Section 3.4) we used H_2O_2 as the photolytic source of OH. In these experiments, HO_2 was also formed and we therefore report the sensitivity (relative to HNO_3) of TPEFS to both HO_2 and H_2O_2.

The experiments on NO, NO_2, HO_2 and H_2O_2 are described in Sections 3.3.1–3.3.4, the results are summarized in Table 1.

3.3.1 NO emission spectrum. In Fig. 6 (upper panel), we present the dispersed NO fluorescence emission (recorded 45 ns after the 193 nm laser pulse) observed upon 193 nm excitation of NO in N_2. Vibronic transitions were assigned using LIFBASE.[35] In Fig. S1 (ESI†) we present absorption cross-sections (185–230 nm) of NO obtained at a spectral resolution of 0.16 nm (as derived from the measured full width (at half maximum) of the 253.65 nm line from a low-pressure Hg lamp). The spectrum was recorded at 19 torr of N_2 with [NO] = 3.1 × 10^{16} molecule cm^{-3} using a 10 cm absorption cell. In this wavelength range, the NO spectrum shows discrete transitions from the ground state to the A, B, C and D electronic states which were assigned using LIFBASE.[35] In Fig. S1 (ESI†), we also indicate the position of the 193 nm ArF laser pulse which lies between the NO absorption features centered around ∼191 nm and ∼195 nm, thus highlighting the lack of NO absorption at the excitation wavelength. At 193 nm, the single-photon absorption cross-section of NO is very low (see Table 1).

Shibuya and Stuhl[39] and Hack *et al.*[40] measured the dispersed fluorescence from a few mTorr of pure NO upon excitation with an ArF laser and reported that the emission (in the 200 to 300 nm range) arose mainly from the $B^2\Pi(v' = 7)$ state, but identified weaker features from the adjacent $A(v' = 3)$ and $C(v' = 0)$ states. Shibuya and Stuhl hypothesized that at 193 nm the absorption arose from the transition from high rotational states (R_{11}, P_{11}, Q_{11}, R_{22} and P_{22}) of the ground state ($X^2\Pi$, $v'' = 0$) to the $B2\Pi(v' = 7)$ state.

Additionally, we measured the dependence of the NO fluorescence signal (as measured through the (310 ± 5) nm interference filter and PMT) as a function of the 193 nm laser energy, which is displayed in Fig. S2 (ESI†). There is a strictly proportional dependence of the NO fluorescence signal as a function of E_{193nm}, which (given the weak absorption of NO at this wavelength) may indicate that the process leading to NO fluorescence involves one photon.

In Fig. S3 (ESI†), we display a series of spectra showing the effect of changing bath gas (He to N_2) and of adding O_2 on the distribution of the NO emission lines upon 193 nm excitation of either NO or NO_2. All spectra were recorded at a total pressure of 65 torr with similar concentrations of either NO or NO_2 ([NO] = 2.6 × 10^{15} molecule cm^{-3}, [NO_2] = 2.1 × 10^{15} molecule cm^{-3}) and [O_2] = 4.0 × 10^{16} molecule cm^{-3}.

In Fig. S3a (ESI†) (NO_2 excitation) we observed that the fluorescence emission is ∼5 times more intense in He than in N_2 for the $A(v' = 0) \rightarrow X$ vibrational series. For NO (Fig. S3b, ESI†), we also observed a stronger quenching effect of He relative to N_2 but observed that in He fluorescence was mainly from the $A(v' = 3)$ electronic state while in N_2 it was from the $A(v' = 0)$ state.

The relative intensity of the emission lines indicates that 85% of the vibrational population was located in the $A(v' = 3)$ state. The replacement of He with N_2 leads to the depopulation, through vibrational energy transfer, of the $A(v' = 3)$ electronic state to form $A(v' = 0, 1, 2)$. We did not observe any evidence of emission down from the $B^2\Pi(v' = 7)$ state as reported previously[39,40] however it appears that under our pressure and bath gas conditions that the $B^2\Pi(v' = 7)$ is quenched down to the observed $A^2\Sigma(v' = 3)$ state in agreement with Hack *et al.*[40] We note that the quenching rate constants were reported to be larger for N_2 (see Settersen *et al.*[41] and references therein) than for He.[42,43]

In Fig. S3c to f (ESI†), we present spectra highlighting the strong O_2 quenching effect on NO fluorescence from both NO_2 and NO excitation.

We also examined the quenching of NO fluorescence (as measured by the PMT through the (310 ± 5) nm interference filter) by O_2. As shown in Fig. 6, in this wavelength window, NO fluorescence arises from NO $A(v' = 0, 1, 2, 3)$ emission to the ground state. In Fig. S4 (ESI†) we show the relative change in fluorescence intensity while the concentration of O_2 was varied from 0 to 4 × 10^{17} molecule cm^{-3} (in N_2 bath gas at a total pressure of 60 torr). From this we derive a quenching rate constant for O_2 of (1.5 ± 0.1) × 10^{-10} cm^3 molecule^{-1} s^{-1}, where the uncertainty is 2σ statistical only (more details in ESI†). This result is in excellent agreement with previous measurements which reported a quenching rate constant for O_2 of 1.5 × 10^{-10} cm^3 molecule^{-1} s^{-1} (see Nee *et al.*[42] and references therein) for NO (A, $v' = 0$). Quenching rate constants were reported as being only weakly dependent on the vibrational level of the A state, with values of k_q within 30% for (A, $v' = 0, 1, 2, 3$) for N_2 and O_2.[42] Our experiments indicate that the numerous quenching rate constant determinations reported in the literature can reproduce our observations at 310 nm.

3.3.2 NO_2 emission spectrum. At 193 nm, the single-photon absorption cross-section of NO_2 is not accurately known with reported values ranging from 2.7 to 5.4 × 10^{-19} cm^2 molecule^{-1},[44] the most recent measurement reported a cross-section of (2.9 ± 1.2) × 10^{-19} cm^2 molecule^{-1} at this wavelength.[45]

Excitation of NO_2 at 193 nm (6.42 eV) leads to its photodissociation to vibrationally excited, electronic ground-state NO($X^2\Pi$) and both O(^1D) and O(^3P)[37,46] as well as N(^4S) and O_2.[47] As shown in Fig. 6 (lower panel), upon excitation of NO_2 at 193 nm, we observed fluorescence emission from NO($A^2\Sigma^+$), as previously reported.[48]

The energy thresholds for the formation of NO $A^2\Sigma^+$ and NO $B^2\Pi$ are 8.60 and 8.75 eV respectively.[49–51] Welge[52] reported the formation of NO($A^2\Sigma^+$ and $B^2\Pi$) after exciting NO_2 to Rydberg

6402 | *Phys. Chem. Chem. Phys.*, 2021, **23**, 6397–6407

This journal is © the Owner Societies 2021

PCCP

Paper

states at 116.5 nm (10.64 eV), 123.6 nm (10.03 eV) and 129.5 nm (9.57 eV) but not at 147 nm (8.43 eV). This indicates that single-photon processes at 193 nm cannot explain the formation of $NO(A^2\Sigma^+)$. On the other hand, simultaneous absorption of two-photons at 193 nm (12.84 eV) appears unlikely to be the source of $NO(A^2\Sigma^+)$ as the ionization energy threshold for the formation of NO^+ is only 12.38 eV.[51] We conclude that a sequential, two-photon absorption mechanism involving a sufficiently long-lived intermediate state (*i.e.* similar to the formation of excited OH in the 2-photon photolysis of HNO_3) might be at the origin of the observed $NO(A^2\Sigma^+)$ in NO_2 photolysis at 193 nm.

3.3.3 Relative TPEFS sensitivity of NO, NO_2 and HNO_3. Initial experiments indicated that the TPEFS detection of HNO_3 around 310 nm (*i.e.* non-dispersed fluorescence) was orders of magnitude more sensitive than for NO or NO_2. In order to extend the dynamic range to measure relative signals from NO, NO_2 and HNO_3 under the same settings (*i.e.* PMT voltage) we reduced the sensitivity (by a factor of 5.4) when monitoring signals from HNO_3 by adding a BG26 optical filter in front of the PMT and using concentrations of HNO_3 that were roughly 10 times smaller than those of NO and NO_2: $[HNO_3] = 0.2–1.2 \times 10^{13}$ molecule cm^{-3}, $[NO] = 2.1–9.9 \times 10^{13}$ molecule cm^{-3}, $[NO_2] = 2.1–8.5 \times 10^{13}$ molecule cm^{-3}. Under these conditions, saturation of the signal at the PMT was avoided when using HNO_3 although the TPEFS signals observed were still roughly 100 times larger for HNO_3 than for NO and NO_2.

In Fig. 7, we present calibration curves in which TPEFS signals are plotted as a function of NO, NO_2 and HNO_3 concentrations.

Note that the right y-axis (for NO and NO_2 detection) is scaled by a factor 0.01 compared to that for HNO_3 (left y-axis). Concentrations of NO_2 and HNO_3 were obtained by *in situ* optical absorption (Section 2.2), whereas the concentration of NO was derived from the mixing ratio in the storage bulb, its
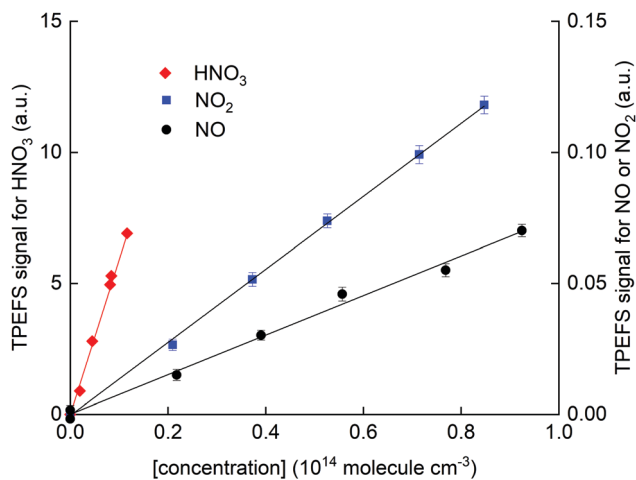
dilution in bath gas and the total pressure. The solid-line fits to the data indicate a sensitivity for detection of NO relative to HNO_3 of $(3 \pm 1) \times 10^{-3}$ in N_2. The values obtained in air and He were $(5 \pm 1) \times 10^{-4}$ and $<10^{-4}$, respectively.

The lower relative sensitivity in air compared to N_2 is readily explained by the more efficient quenching of O_2 on NO fluorescence than on OH fluorescence. It is also amplified by the very low quenching rate constant of NO fluorescence by N_2.[41]
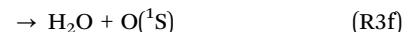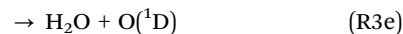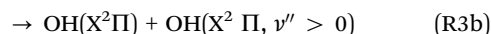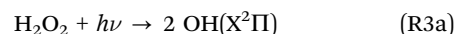
In He, the TPEFS sensitivity to HNO_3 increased (compared to N_2) much more than it did for NO or NO_2. This forced us to reduce the PMT-voltage when monitoring HNO_3 whereby usable signals from NO and NO_2 were only obtained by adding much larger concentrations for which fluorescence self-quenching was an issue. In He we were thus unable to extend the dynamic range of the experiment to measure signals from HNO_3 and NO or NO_2 under the same conditions and we only report a lower limit of 10^{-4} to the relative sensivity.

In order to perform similar experiments on NO_2, we initially used diluted NO_2 samples. However, we found that a small but variable fraction (around 0.1–1%) of the NO_2 was converted to HNO_3 on the inlet and reactor surfaces. We therefore generated NO_2 *in situ* in a pre-reactor by reacting NO with O_3. The latter, at a concentration of 1.0×10^{13} molecule cm^{-3}, was generated by the photolysis of O_2 at 185 nm using a Hg lamp.

The conversion of NO to NO_2 was 92 to 95%. We thus obtained a relative detection efficiency (in N_2) of NO_2 compared to HNO_3 of $(5 \pm 3) \times 10^{-3}$.

3.3.4 Detection of H_2O_2. The single-photon cross-section of H_2O_2 at 193 nm is 6.1×10^{-19} cm^2 molecule^{-1}.[23] In a series of experiments in 50 torr N_2 at ~ 298 K we observed a linear dependence of the TPEFS signal on the H_2O_2 concentration (varied from 0.11 to 1.1×10^{16} molecule cm^{-3}) as shown in Fig. S5 (ESI†). The TPEFS detection sensitivity of H_2O_2 relative to that of HNO_3 of was found to be $(6 \pm 2) \times 10^{-5}$, where the uncertainty is 2σ statistical only.

Previous studies on the VUV photolysis of H_2O_2[53–56] indicate that OH, H and O-atoms are formed:

$$H_2O_2 + h\nu \rightarrow 2\ OH(X^2\Pi) \tag{R3a}$$

$$\rightarrow OH(X^2\Pi) + OH(X^2\ \Pi, v'' > 0) \tag{R3b}$$

$$\rightarrow H(^2S) + HO_2 \tag{R3c}$$

$$\rightarrow H_2O + O(^3P) \tag{R3d}$$

$$\rightarrow H_2O + O(^1D) \tag{R3e}$$

$$\rightarrow H_2O + O(^1S) \tag{R3f}$$

At $\lambda < 198$ nm excitation, the main dissociation pathways lead to two OH (R5a and R5b) and to $H(^2S)$ atom and HO_2 (R5c). At 193 nm, the yields for the OH + OH channel (R5a) and the H + HO_2 (R5c) are 0.8 and 0.2, respectively and an upper limit of 0.15 was given for the formation of vibrationally excited $OH(X^2\ \Pi, v'' > 0)$ (R5b).[54] The yields of O-atoms are very low with upper limits of 0.001 for $O(^3P) + O(^1D)$ and 0.02 for $O(^1S)$ channels. OH(A) is formed at wavelength below 172 nm.[57]

Fig. 7 HNO_3 TPEFS signal (left y-axis) and NO and NO_2 TPEFS signal (right y-axis) as a function of concentration. These results were obtained in N_2 (62 torr) and at room temperature (298 ± 2 K).

This journal is © the Owner Societies 2021

Phys. Chem. Chem. Phys., 2021, **23**, 6397–6407 | 6403

Formation of OH(A), has however been observed in the two-photon excitation of H_2O_2 at 193 nm[58,59] which, *via* analysis of the state resolved internal distribution of OH(A), was demonstrated to originate from a resonant, 2-photon sequential absorption process.

3.3.5 Detection of HO_2. HO_2 was formed in the 248 nm photolysis of H_2O_2 whereby the initially formed OH radicals were converted to HO_2 in (R4).
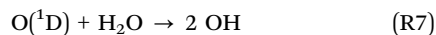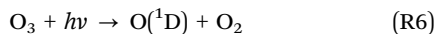
$$OH + H_2O_2 \rightarrow HO_2 + H_2O \qquad (R4)$$
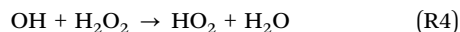
The sensitivity for detection of HO_2 at 193 nm was examined in 60 torr of N_2 with $[H_2O_2] = 2.4 \times 10^{15}$ molecule cm^{-3}. The photon density at 248 nm was measured using a calibrated Joulemeter as 6.8×10^{16} photon cm^{-2}. Under these conditions, $\sim 1.6 \times 10^{13}$ molecule cm^{-3} of HO_2 were generated. The observed TPEFS signal was modelled as the sum of the signals originating directly from H_2O_2 and from HO_2 formed in R4. The kinetic model included R4 and R5 with diffusion coefficients for OH and HO_2 set to 30 s^{-1}. In Fig. S6 (ESI†), we show the signal expected when assuming that HO_2 was not detected. The slight depletion in signal at time = zero is explained by the loss of H_2O_2 by photolysis ($\sim 1.5\%$) and in the subsequent OH + H_2O_2 reaction. From this data we were only able to report an upper limit HO_2 detection sensitivity (relative to HNO_3) of $(3.2 \pm 1.2) \times 10^{-4}$ (2σ statistical only, including a 15% uncertainty on the photon density).

3.4 Rate coefficient for the OH + NO_2 reaction

Rate coefficients for OH + NO_2 were measured by both conventional pulsed laser photolytic formation of OH with its detection in real time by laser induced fluorescence (PLP-LIF, with 282 nm excitation of OH and PLP-TPEFS with 193 nm excitation for detection of the HNO_3 product).

OH radicals were generated either in the 248 nm photolysis of H_2O_2 (R5) or by the 248 nm photolysis of O_3 in the presence of H_2O (R6 and R7).

$$H_2O_2 + h\nu \rightarrow 2\ OH \qquad (R5)$$

$$O_3 + h\nu \rightarrow O(^1D) + O_2 \qquad (R6)$$

$$O(^1D) + H_2O \rightarrow 2\ OH \qquad (R7)$$

The concentrations used were $[H_2O_2] \sim 1 \times 10^{14}$ molecule cm^{-3}, $[O_3] = (2-7) \times 10^{13}$ molecule cm^{-3} and $[H_2O] = (1.5-6.0) \times 10^{16}$ molecule cm^{-3} (corresponding to a mixing ratio of $\sim 4.2\%$ at the total pressure of 50 to 200 torr, see Table 2). Using a laser-fluence of ~ 50 mJ cm^{-2}, $1-3 \times 10^{12}$ molecule cm^{-3} [OH] were generated per pulse such that the experiments were conducted under pseudo-first order conditions (*i.e.* $[NO_2] \gg [OH]$).

We observed that small amounts of NO_2 ($<0.1\%$) were converted into HNO_3 on the surfaces of the reactor adding a background signal to the kinetics profile. The effect became more pronounced when water vapour was added to the reactor where as much as a few percent of NO_2 were converted to HNO_3. We note that the build-up of background HNO_3 occurred on a longer time scale ($\sim 2-3$ hours) than the time

Table 2 Determination of k_2 in air

Pressure (torr)	H_2O (%)	k_2 (10^{-12} cm^3 molecule^{-1} s^{-1})
O_3/H_2O as OH precursor		
50	4.5	(3.2 ± 0.7)
100	4.1	(4.5 ± 0.4)
150	3.8	(5.7 ± 0.8)
200	4.5	(6.6 ± 0.3)
H_2O_2 as OH precursor		
50	0	(2.3 ± 0.3)
100	0	(3.9 ± 0.3)
100	0	$(4.0 \pm 0.1)^a$

^{a} OH LIF measurement. Errors are 2σ statistical only.

necessary to gather the data necessary to derive a rate constant for one particular set of conditions. However, it did prevent conducting a long-time series of measurements (*e.g.* over the course of a day) as the background became too large and the reactor cell needed to be flushed with dry N_2 for several hours to return to favourable conditions. The use of NaHCO3 to coat the surface was impractical in these experiments as its efficiency to remove HNO_3 also changed over time.

In both schemes, OH is generated quasi-instantaneously compared to its loss rate and the time profiles for OH loss and HNO_3/HOONO production in the cell are then given by:

$$[OH]_t = [OH]_0 \exp(-[k_2[NO_2] + d_{OH}]t) \qquad (3)$$

$$[HNO_3]_t = \alpha C(\exp(-d_{HNO_3}t) - \exp(-[k_2[NO_2] + d_{OH}]t)) \qquad (4)$$

$$[HOONO]_t = (1 - \alpha)C(\exp(-d_{HOONO}t) - \exp(-[k_2[NO_2] + d_{OH}]t)) \qquad (5)$$

where k_2 is the rate coefficient for reaction (R2), d_{OH} and d_{HNO_3} are first-order rate constants (s^{-1}) for the diffusive loss of OH and HNO_3 from the reaction volume, respectively and C is equal to $[OH]_0(k_2[NO_2] + d_{OH})/(k_2[NO_2] + d_{OH} + d_{HNO_3})$. We do not know if TPEFS detects HOONO but note that, to a very good approximation, the first-order constant for formation of HOONO will be the same as for HNO_3 as both are very long-lived compared to the time-scale of the decay of OH. Only the absolute concentrations of HNO_3 and HOONO are defined by the branching ratio and thus the kinetic parameters would not be impacted whether HOONO is detected or not.

The pseudo-first-order loss rate coefficient for OH is:

$$k_2' = k_2[NO_2] + d_{OH} \qquad (6)$$

Experiments to derive k_2 were carried out at room temperature and at a number of different pressures of air (50–200 torr) using the two different OH precursors described above. We worked in air rather than in N_2 as this improves the relative sensitivity to HNO_3 compared to NO_2.

Fig. 8 shows time profiles for both OH decay (upper panel) and HNO_3 production (lower panel) obtained for the same chemical system using H_2O_2 as a precursor. The HNO_3 TPEFS signals displayed were accumulated for 40 scans (~ 10 min) while OH LIF signal were accumulated for 25 scans (~ 5 min). The profiles were obtained by computer-controlled variation of

6404 | *Phys. Chem. Chem. Phys.*, 2021, **23**, 6397–6407
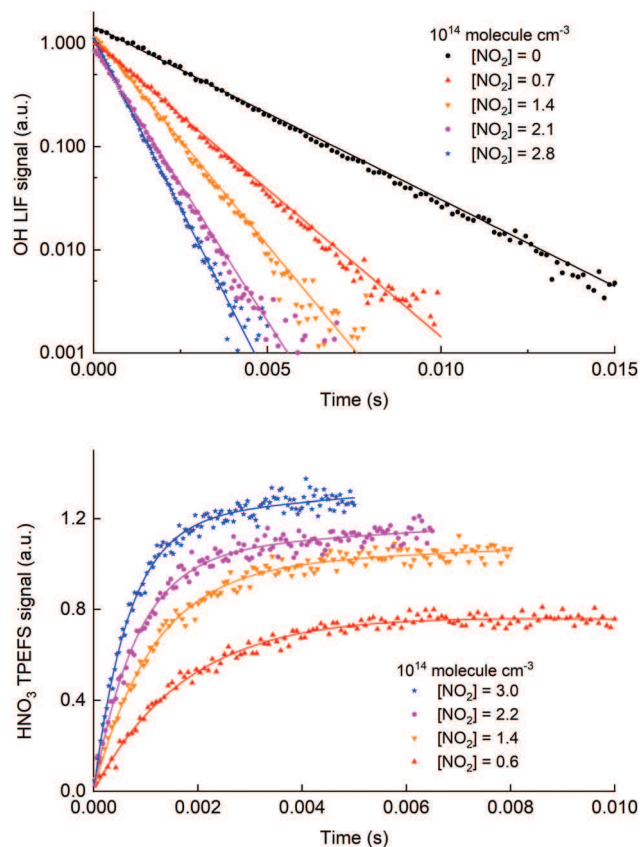
This journal is © the Owner Societies 2021

Fig. 8 Time dependent signals from OH (upper panel, LIF) and HNO₃ (lower panel, TPEFS) obtained in measurements at 100 torr of air using H_2O_2 as a OH precursor. The solid lines are fits to the OH (eqn (3)) and HNO₃ signals (eqn (4)). The reaction time for the HNO₃ formation datasets was adjusted (*i.e.* shorter at high [NO₂]) to get sufficient datapoints in the early part of the profile.

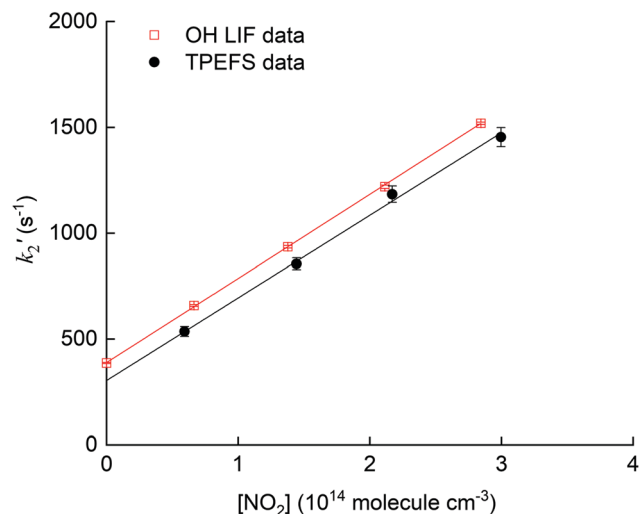Fig. 9 Plot of k_2' versus [NO₂] for the reaction (R2) of OH with NO₂ at 100 torr of air using H_2O_2 as OH precursor. The solid lines represent a linear regression returning $k_2 = (4.0 \pm 0.1) \times 10^{-12}$ cm³ molecule⁻¹ s⁻¹ using OH detection by LIF (red line) and $k_2 = (3.9 \pm 0.3) \times 10^{-12}$ cm³ molecule⁻¹ s⁻¹ using HNO₃ detection by TPEFS (black line). Error bars are 2σ statistical only.
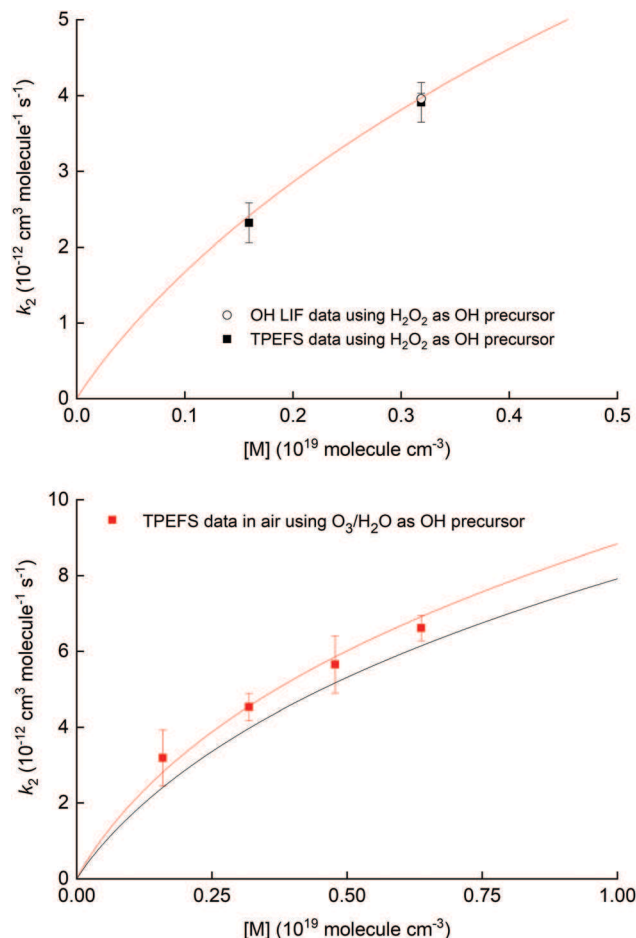

Fig. 10 Upper panel: Measurement of k_2 for the OH reaction with NO₂ in air using 248 nm photolysis of H_2O_2 as a OH precursor and either TPEFS detection of HNO₃ or conventional LIF detection of OH. The solid red line is a fall-off parameterisation (see ESI†). Lower panel: Measurement of k_2 for the OH reaction with NO₂ in air using 248 nm photolysis of O_3–H_2O to generate OH. The solid red line is a fall-off parameterization (see the ESI†) using a mixing ratio for H_2O of 4.2% while the solid black line corresponds to the same parametrisation in dry air.

the delay-time between the 248 nm excimer laser pulse (generating OH at time zero) and either the 282 nm laser exciting OH or the 193 nm excimer-laser exciting HNO₃.

The pseudo first-order rate coefficients, k_2', were obtained by fitting the observed time profiles to eqn (3) and (4) for OH loss and HNO₃ production, respectively. The bimolecular rate coefficients were then obtained by plotting k_2' against [NO₂] as shown in Fig. 9, which displays data from an experiment at a total pressure of 100 torr of air whereby [NO₂] was varied between 0.5 and 3×10^{14} molecule cm⁻³.

The values of k_2 obtained from the slopes of least-squares fits to these datasets are (4.0 ± 0.1) and $(3.9 \pm 0.3) \times 10^{-12}$ cm³ molecule⁻¹ s⁻¹, respectively.

Fig. 10 shows the measured rate coefficients as a function of pressure along with fall-off expression (see the ESI†) used to parameterize data recently measured in this laboratory.[19,20]

The results displayed in the upper panel of Fig. 10 indicate that the rate coefficients obtained using detection of HNO₃

using TPEFS are in excellent agreement (better than 10%) with that obtained using OH-LIF and also with the parameterisation presented in our previous, comprehensive study (using OH-LIF). The lower panel indicates that larger rate coefficients are obtained when using O_3/H_2O as OH-precursor. This observation is entirely consistent with the enhancement of k_2 in the presence of H_2O described in detail by Amedro et al.[19] and the parameterisation of k_2 presented by those authors (red line). Note that the overall aim of the kinetic investigations described in Section 3.4 was not to strengthen the database on the OH + NO_2 reaction, but to show that time resolved detection of HNO_3 by TPEFS can be used to derive accurate rate coefficients. For more details about the OH reaction with NO_2 rate constants measurements, including an extended comparison with previous works and a newly developed parametrization, we invite the interested reader to view our previous studies.[19,20] We are unaware of any reason why TPEFS detection of HNO_3 could not be extended to kinetic studies at e.g. different temperatures.

4. Conclusions

We have characterized the detection of HNO_3 using TPEFS as part of a study to assess its viability for detection of HNO_3 in real-time (e.g. pulsed laser) kinetic studies. We have shown that detection of HNO_3 (via OH(A) emission at ~ 310 nm is orders of magnitude more sensitive than detection NO or NO_2 (via NO* emission) at the same wavelength, especially in air where the quenching of NO fluorescence is most efficient owing to the presence of O_2. As a test case, we have used TPEFS for real-time detection of HNO_3 in the reaction between OH and NO_2. The rate constant obtained (293 K, 50–200 torr) is entirely consistent with that obtained by simultaneously measuring the OH decay and is in very good agreement with the most recent literature values.

Author contributions

DA, TD and JC set up the apparatus, DA, TD and AB performed the experiments. DA analysed the data. JC conceptualised the experiments and helped DA write the manuscript.

Conflicts of interest

There are no conflicts to declare.

Acknowledgements

Notes and references

1 R. Atkinson, D. L. Baulch, R. A. Cox, J. N. Crowley, R. F. Hampson, R. G. Hynes, M. E. Jenkin, M. J. Rossi and J. Troe, Atmos. Chem. Phys., 2004, 4, 1461.

2 A. A. Turnipseed, G. L. Vaghjiani, J. E. Thompson and A. R. Ravishankara, J. Chem. Phys., 1992, 96, 5887.

3 P. Felder, X. F. Yang and J. R. Huber, Chem. Phys. Lett., 1993, 215, 221.

4 A. Schiffman, D. D. Nelson and D. J. Nesbitt, J. Chem. Phys., 1993, 98, 6935.

5 T. L. Myers, N. R. Forde, B. Hu, D. C. Kitchen and L. J. Butler, J. Chem. Phys., 1997, 107, 5361.

6 J. Schlütter and K. Kleinermanns, Chem. Phys. Lett., 1992, 192, 94.

7 A. Jacobs, K. Kleinermanns, H. Kuge and J. Wolfrum, J. Chem. Phys., 1983, 79, 3162.

8 G. H. Leu, C. W. Hwang and I. C. Chen, Chem. Phys. Lett., 1996, 257, 481.

9 Q. Li, R. T. Carter and J. R. Huber, Chem. Phys. Lett., 2001, 334, 39.

10 H. Okabe, J. Chem. Phys., 1980, 72, 6642.

11 M. Suto and L. C. Lee, J. Chem. Phys., 1984, 81, 1294.

12 T. Papenbrock, H. K. Haak and F. Stuhl, Ber. Bunsen-Ges., 1984, 88, 675.

13 R. D. Kenner, F. Rohrer and F. Stuhl, Chem. Phys. Lett., 1985, 116, 374.

14 R. D. Kenner, F. Rohrer, T. Papenbrock and F. Stuhl, J. Phys. Chem., 1986, 90, 1294.

15 T. Papenbrock and F. Stuhl, Atmos. Environ., Part A, 1991, 25, 2223.

16 T. Papenbrock, F. Stuhl, K. P. Müller and J. Rudolph, J. Atmos. Chem., 1992, 15, 369.

17 F. A. F. Winiberg, C. J. Percival and S. P. Sander, Chem. Phys. Lett., 2019, 3, 100029.

18 K. Dulitz, D. Amedro, T. J. Dillon, A. Pozzer and J. N. Crowley, Atmos. Chem. Phys., 2018, 18, 2381.

19 D. Amedro, M. Berasategui, A. J. C. Bunkan, A. Pozzer, J. Lelieveld and J. N. Crowley, Atmos. Chem. Phys., 2020, 20, 3091.

20 D. Amedro, A. J. C. Bunkan, M. Berasategui and J. N. Crowley, Atmos. Chem. Phys., 2019, 19, 10643.

21 A. K. Mollner, S. Valluvadasan, L. Feng, M. K. Sprague, M. Okumura, D. B. Milligan, W. J. Bloss, S. P. Sander, P. T. Martien, R. A. Harley, A. B. McCoy and W. P. L. Carter, Science, 2010, 330, 646.

22 J. Troe, J. Phys. Chem. A, 2012, 116, 6387.

23 IUPAC, Task Group on Atmospheric Chemical Kinetic Data Evaluation, (Ammann, M., Cox, R. A., Crowley, J. N., Herrmann, H., Jenkin, M. E., McNeill, V. F., Mellouki, A., Rossi, M. J., Troe, J. and Wallington, T. J.), http://iupac.pole-ether.fr/index.html.).

24 M. Wollenhaupt, S. A. Carl, A. Horowitz and J. N. Crowley, J. Phys. Chem., 2000, 104, 2695.

25 A. C. Vandaele, C. Hermans, S. Fally, M. Carleer, R. Colin, M. F. Merienne, A. Jenouvrier and B. Coquart, J. Geophys. Res.: Atmos., 2002, 107, 4348.

26 G. L. Vaghjiani and A. R. Ravishankara, J. Geophys. Res.: Atmos., 1989, 94, 3487.

27 F. Biaume, J. Photochem., 1973–1974, 2, 139.

28 P. H. Wine, A. R. Ravishankara, N. M. Kreutter, R. C. Shah, J. M. Nicovich, R. L. Thompson and D. J. Wuebbles, J. Geophys. Res.: Atmos., 1981, 86, 1105.

6406 | Phys. Chem. Chem. Phys., 2021, 23, 6397–6407

This journal is © the Owner Societies 2021

29 C. A. Cantrell, A. Zimmer and G. S. Tyndall, *Geophys. Res. Lett.*, 1997, **24**, 2195.

30 R. A. Copeland and D. R. Crosley, *J. Chem. Phys.*, 1986, **84**, 3099.

31 A. E. Bailey, D. E. Heard, P. H. Paul and M. J. Pilling, *J. Chem. Soc., Faraday Trans.*, 1997, **93**, 2915.

32 R. A. Copeland and D. R. Crosley, *Chem. Phys. Lett.*, 1984, **107**, 295.

33 R. A. Copeland, M. J. Dyer and D. R. Crosley, *J. Chem. Phys.*, 1985, **82**, 4022.

34 K. R. German, *J. Chem. Phys.*, 1975, **62**, 2584.

35 J. Luque and D. R. Crosley, LIFBASE (version 1.5) http://www.sri.com/cem/lifbase, 1999.

36 R. D. Kenner, F. Rohrer and F. Stuhl, *J. Phys. Chem.*, 1986, **90**, 2635.

37 F. Sun, G. P. Glass and R. F. Curl, *Chem. Phys. Lett.*, 2001, **337**, 72.

38 J. N. Crowley, F. G. Simon, J. P. Burrows, G. Moortgat, K. M. E. Jenkin and R. A. Cox, *J. Photochem.*, 1991 **60**, 1.

39 K. Shibuya and F. Stuhl, *J. Chem. Phys.*, 1982, **76**, 1184.

40 W. Hack, R. K. Sander, J. J. Valentini and N. S. Nogar, *Mol. Phys.*, 1985, **56**, 977.

41 T. B. Settersten, B. D. Patterson and C. D. Carter, *J. Chem. Phys.*, 2009, **130**, 204302.

42 J. B. Nee, C. Y. Juan, J. Y. Hsu, J. C. Yang and W. J. Chen, *Chem. Phys.*, 2004, **300**, 85.

43 J. Few and G. Hancock, *Phys. Chem. Chem. Phys.*, 2014, **16**, 11047.

44 W. Schneider, G. K. Moortgat, G. S. Tyndall and J. P. Burrows, *J. Photochem. Photobiol., A*, 1987, **40**, 195.

45 J. M. Sun, M. Y. Zhang and T. S. Liu, *J. Geophys. Res.: Atmos.*, 2001, **106**, 10325.

46 G. Hancock and M. Morrison, *Mol. Phys.*, 2005, **103**, 1727.

47 T. Nakayama, K. Takahashi, Y. Matsumi and K. Shibuya, *J. Phys. Chem. A*, 2005, **109**, 10897.

48 H. K. Haak and F. Stuhl, *J. Photochem.*, 1981, **17**, 69.

49 K. P. Huber and G. Herzberg, *Molecular spectra and molecular structure IV. Constants of diatomic molecules*, Van Nostrand Reinhold Company Inc., New York, 1st edn, 1979.

50 R. Jost, J. Nygard, A. Pasinski and A. Delon, *J. Chem. Phys.*, 1996, **105**, 1287.

51 I. Wilkinson, I. A. Garcia, B. J. Whitaker, J.-B. Hamard and V. Blanchet, *Phys. Chem. Chem. Phys.*, 2010, **12**, 15766.

52 K. H. Welge, *J. Chem. Phys.*, 1966, **45**, 1113.

53 U. Gerlach-Meyer, E. Linnebach, K. Kleinermanns and J. Wolfrum, *Chem. Phys. Lett.*, 1987, **133**, 113.

54 G. Vaghjiani, A. A. Turnipseed, R. F. Warren and A. R. Ravishankara, *J. Chem. Phys.*, 1992, **96**, 5878.

55 Y. Inagaki, Y. Matsumi and M. Kawasaki, *Bull. Chem. Soc. Jpn.*, 1993, **66**, 3166.

56 T. Nakayama, K. Takahashi and Y. Matsumi, *Int. J. Chem. Kinet.*, 2005, **37**, 751.

57 M. Suto and L. C. Lee, *Chem. Phys. Lett.*, 1983, **98**, 152.

58 H. Gölzenleuchter, K.-H. Gericke and F. Josef Comes, *Chem. Phys. Lett.*, 1985, **116**, 61.

59 C. B. McKendrick, E. A. Kerr and J. P. T. Wilkinson, *J. Phys. Chem.*, 1984, **88**, 3930.

This journal is © the Owner Societies 2021

Phys. Chem. Chem. Phys., 2021, **23**, 6397–6407 | **6407**